nature communications

Article

https://doi.org/10.1038/s41467-026-77862-w

Wafer-scale conformal metasurface optics

Received: 12 January 2026

Accepted: 7 September 2026

Published online: 18 September 2026

Check for updates

Louis Martin-Monier[1], Sehui Chang[2,3], Johannes E. Fröch[4], Zhaoyi Li[1] ✉, Luigi Ranno[1], Khoi Phuong Dao[1], Akira Ueno[1], Jia Xu Brian Sia[1], Hanyu Zheng[1,5], Padraic Burns[5], Tian Gu[1,5] ✉, Young Min Song[2,3] ✉, Arka Majumdar[4,6] & Juejun Hu[1,5]

Curved and conformal optics provide additional geometric degrees of freedom that enable enhanced optical performance while satisfying non-optical constraints such as ergonomics, aerodynamics, and wearability. However, existing fabrication approaches for curved metasurfaces are limited in scalability, geometry control, and alignment accuracy. Here we show a scalable fabrication strategy for curved and conformal metasurface optics based on thermoforming, an industry-standard manufacturing process for thermoplastics. Our approach enables wafer-scale production of highly curved metasurfaces with millimeter-level radii of curvature and micron-level alignment precision. We develop a predictive thermorheological model that accurately captures and compensates for the large deformations induced during thermoforming, preserving the intended optical response and enabling diffraction-limited performance. As demonstrations, we realize freestanding curved metalenses, conformal refractive-metasurface hybrid optics, and an artificial compound eye with a wide field of view, reduced aberrations, and uniform imaging performance. These results establish thermoforming as a scalable manufacturing platform for next-generation conformal photonic systems.

Flat optics exemplified by metasurfaces and diffractive optical elements offer major size, weight, and cost advantages over traditional bulk optics and are seeing growing commercial deployment in recent years. Taking advantage of their ultrathin form factor, flat optics can also assume non-planar forms, either as standalone elements or as a conformal layer integrated on curved substrates[1–3]. The added geometric degrees of freedom have been proven to significantly enhance their optical performance and functionality compared to flat counterparts[4–7]. For example, conformal integration of metasurfaces with freeform reflective[8] or refractive[9,10] optics can improve aberration correction and extend the achievable field of view, enabling enhanced imaging quality with the same or even reduced number of optical elements (refer to examples in Supplementary Note 1). Curved metasurfaces can also function as lightweight, high-numerical-aperture compact objectives for miniature cameras or as beam-shaping elements embedded within lamp domes and lighting modules, where curvature enables tailored angular emission profiles without increasing system complexity.

Beyond purely optical considerations, decoupling the physical shape of a meta-optical component from its optical phase function enables independent optimization with respect to mechanical, aerodynamic, ergonomic, and industrial design constraints. Conformal metasurfaces can therefore be integrated onto drone fuselages, missile domes, and vehicle body panels to preserve streamlined aerodynamics[11], or onto helmets, visors, eyewear frames, curved display panels, and wearable platforms to meet ergonomic

[1]Department of Materials Science & Engineering, Massachusetts Institute of Technology, Cambridge, MA, USA. [2]School of Electrical Engineering, Korea Advanced Institute of Science and Technology, Daejeon, Republic of Korea. [3]GIST InnoCORE AI-Nano Convergence Institute for Early Detection of Neurodegenerative Diseases, Gwangju Institute of Science and Technology, Gwangju, Republic of Korea. [4]Department of Electrical and Computer Engineering, University of Washington, Seattle, WA, USA. [5]2Pi Inc., Cambridge, MA, USA. [6]Department of Physics, University of Washington, Seattle, WA, USA. ✉e-mail: zhaoyili@mit.edu; gutian@mit.edu; ymsong@kaist.ac.kr

requirements[12,13]. Similarly, metasurfaces can be incorporated into curved housings for LiDAR and free-space communication systems, or embedded directly into thermoplastic packaging and product enclosures where curvature is dictated by structural or aesthetic considerations. In such scenarios, curvature is often defined by non-optical constraints, and conformal metasurfaces provide a means to embed advanced optical functionality without compromising the underlying form factor.

Current fabrication methods for conformal metasurfaces and diffractive optical elements suffer from significant limitations in scalability, geometric control, and alignment accuracy. While laser[14] or electron beam[8] direct-write techniques have been adapted for patterning on curved substrates, their inherently low throughput renders them unsuitable for large-scale manufacturing. Alternative strategies employ elastomeric stamps capable of conforming to non-planar surfaces for direct nanoimprint lithography[15–17]. These direct patterning approaches are constrained to gently curved surfaces, with radii of curvature generally exceeding several centimeters. In addition, achieving micron-scale alignment accuracy is challenging for soft nanoimprint processes on curved substrates, as elastomeric stamps are susceptible to deformation, distortion, and registration errors during contact and release. Another common approach involves fabricating metasurfaces on flat, rigid substrates followed by transfer to elastomeric carriers for conformal integration[18–21]. Precise alignment, which is crucial to assembly of optical systems involving these non-planar elements, is however, challenging as elastomers are prone to mechanical deformation. Although non-elastomeric polymer substrates have also been used[22,23], their limited stretchability restricts the achievable curvature to one-dimensional bending.

To circumvent the limitations of the existing methods, we turn to thermoforming, an industry-proven technique renowned for its scalability and reliability in high-volume production of thermoplastic components. In thermoforming, a rigid thermoplastic sheet that is initially stiff and dimensionally stable at room temperature is heated to a pliable state where its viscosity falls within the range of 10^4 to 10^6 Pa·s. At this viscoelastic condition, the sheet can be shaped into a desired form using a mold through vacuum, pressure, or mechanical forming. Upon cooling, the material regains its original rigidity, permanently retaining the newly formed geometry. Inspired by the thermoforming process, we developed a curved and conformal metasurface fabrication strategy that is fully compatible with high-throughput wafer-foundry processes, including deep-ultraviolet (DUV) lithography and nanoimprint techniques. Our thermoforming-based method enables large-area shaping of conformal optics with high dimensional fidelity, even for geometries featuring tight, millimeter-scale curvature. The inherent mechanical rigidity and dimensional stability of the thermoplastic sheet further support precise wafer- or panel-level alignment, ensuring accurate pattern registration throughout the optics assembly process. Together, these advantages (Table 1) position our approach as a scalable and industrially viable solution for next-generation conformal photonic systems. In this work, we develop a thermoforming-based fabrication strategy for wafer-scale curved and conformal metasurface optics, establish a predictive thermorheological model for deformation-aware design, and demonstrate freestanding curved metalenses, conformal refractive-metasurface hybrid optics, and a bioinspired compound eye.

Results

The fabrication process is schematically depicted in Fig. 1a. The process begins with the deposition and lithographic patterning of a high-refractive-index layer into metasurface structures on a flat silica glass wafer. In this study, hydrogenated amorphous silicon (a-Si) is used as the meta-atom material, though the overall approach is readily adaptable to other metasurface platforms. After a brief oxygen plasma treatment to improve surface wettability, a solution of thermoplastic polymer (polyvinyl chloride (PVC) dissolved in cyclohexanone in our study) is drop-cast and spin-coated onto the patterned wafer. PVC is selected primarily for its strong resistance to hydrofluoric acid, which enables clean release of the metasurface without chemical damage, as well as for its relatively low glass transition temperature that facilitates thermoforming with reduced thermal nonuniformity. In addition, PVC is widely adopted in industrial thermoforming due to its low cost and high processing tolerance, making it an attractive material for scalable manufacturing. Subsequent thermal annealing forms a thin encapsulation layer, typically ~2 μm thick, conformally covering the a-Si metasurface. A thermoplastic PVC sheet of tailored thickness (typically several hundred microns) is then thermally bonded onto this encapsulated layer. To release the structure, the thermoplastic-embedded metasurface is separated from the substrate using a wet etchant that selectively attacks the a-Si/glass interface. The rapid lateral etching enables clean delamination while minimizing chemical damage to the a-Si nanostructures.

The released structure, now in the form of a rigid thermoplastic substrate, is subsequently shaped via the thermoforming process. Precise alignment between the metasurface-embedded substrate and the mold is essential for achieving high-quality optical performance. In this study, we developed an alignment protocol based on interferometric microscopy to ensure micron-level placement accuracy. Importantly, because the form factor and mechanical rigidity of the thermoplastic substrate closely match those of conventional glass wafers, standard wafer- or panel-level alignment techniques commonly used in semiconductor manufacturing can also be readily applied. The aligned substrate-mold assembly is then transferred to a commercial benchtop thermoforming machine, where the thermoplastic substrate is heated to a pliable state and vacuum is applied through the perforated base to conform it onto the mold surface. After cooling, the molded metasurface can either be demolded to serve as a freestanding optical element or remain permanently bonded to the rigid mold—such as a refractive lens—to create hybrid refractive-metasurface optics. Details of the fabrication process are furnished in Methods.

We demonstrate the scalability of our thermoforming process through a wafer-scale fabrication test. A sparse 5 × 5 array of metasurfaces, each occupying a 2 mm × 2 mm area, was patterned via electron beam lithography on a 6-inch glass wafer. The metasurface structures were subsequently transferred to a 6-inch PVC substrate and thermoformed using the previously described protocol. Off-the-shelf plano-convex lenses mounted on a base plate served as the thermoforming mold. Fig 1b shows interferometric microscope images acquired during the alignment process. The right panel displays concentric Newton's rings centered on the metasurface, indicating optimal alignment with the mold, while the center panel shows misalignment. Using this method, we achieve alignment accuracy within ± 10 μm across the conformal optics, which, according to our simulations (Supplementary Note 2), introduces negligible degradation to the optical performance of the resulting curved metasurfaces. Importantly, this limit is imposed not by the alignment protocol itself but by non-uniform heating and post-forming thermal contraction; both effects could be further mitigated by employing thermoforming systems with enclosed, multi-zone heating to improve temperature uniformity (Supplementary Note 3). Optical profilometry measurements presented in Supplementary Note 4 reveal that the thermoformed component closely replicates the mold surface geometry. Figure 1c presents a cross-sectional scanning electron microscopy (SEM) image of the molded metasurface, confirming that the meta-atoms retain their structural integrity after thermoforming. The apparent tapering of the meta-atom profiles is an artifact resulting from the focused ion beam (FIB) cross-sectioning plane being slightly tilted relative to the local surface normal of the curved polymer substrate. Figure 1d shows a photograph of the fully processed PVC

https://doi.org/10.1038/s41467-026-77862-w

Table 1 | Representative experimental demonstrations of curved and conformal metasurface optics fabrication methods

	Fabrication method	Sample area/size	Freestanding?	2D conformal integration?	Smallest radius of curvature	Alignment accuracy
Adv. Photonics Res. **5**, 2300241 (2024)[14]	Direct laser writing	~12.7 mm diameter lens	No	Yes	56.1 mm	N/A
Sci. Adv. **7**, eabe5112 (2021)[8]	Electron-beam lithography	3 mm^2 patterned aperture on 6 mm diameter concave mirror	No	Yes	~ 8 mm	Micron-level (alignment to fiducials)
Science **349**, 1310-1314 (2015)[29]	Electron-beam lithography on surface topology carved by focused ion beam	~ 30 μm	No	Yes	Tens of microns	Sub-micron
Nano Res. **11**, 2705 (2018)[15]	Nanoimprint	35 mm diameter	No	Yes (gentle curves only)	50 mm (spherical)	N/A
ACS Appl. Mater. Interfaces 11, 26109-26115 (2019)[30]	Nanoimprint	~ 3 cm diameter	Yes	Yes	Several centimeters	N/A
PhotoniX **4**, 18 (2023)[17] *Nat. Food* **5**, 293 (2024)[31]	Nanoimprint	~ 5 cm diameter	Yes	Yes	Several centimeters	N/A
Nat. Commun. **7**, 11618 (2016)[18]	Transfer to elastomer substrates	A few mm^2	No (flexible film requires support)	Yes	4.13 mm (cylindrical)	Manual placement
ACS Photonics **5**, 1762-1766 (2018)[32]	Release of epoxy layer from flat substrate	Few-mm patch on curved object	No (film is flexible, but not in self-supporting shape)	No (bendable film, not stretchable)	6 mm (cylindrical)	Manual placement
Laser Photon Rev **19**, 2401240 (2024)[13]	Release of epoxy layer from flat substrate	Few-mm patch on curved eyeglass	Yes	No (bendable film, not stretchable)	cm-scale	Manual placement
Appl. Phys. Lett. **123**, 231702 (2023)[33]	Release of epoxy layer from flat substrate	cm-scale films	Yes	No (bendable film, not stretchable)	26 mm	N/A
Adv. Sci. **11**, 2407045 (2024)[34]	Transfer printing	cm-scale contact lens	No	Yes	~ 9 mm	Manual placement
This work	Transfer to thermoplastic substrates followed by thermoforming	6″ diameter substrate (wafer-scale)	Yes	Yes	3.2 mm	10 μm

N/A indicates that the corresponding information was not provided in the referenced publication.

https://doi.org/10.1038/s41467-026-77862-w

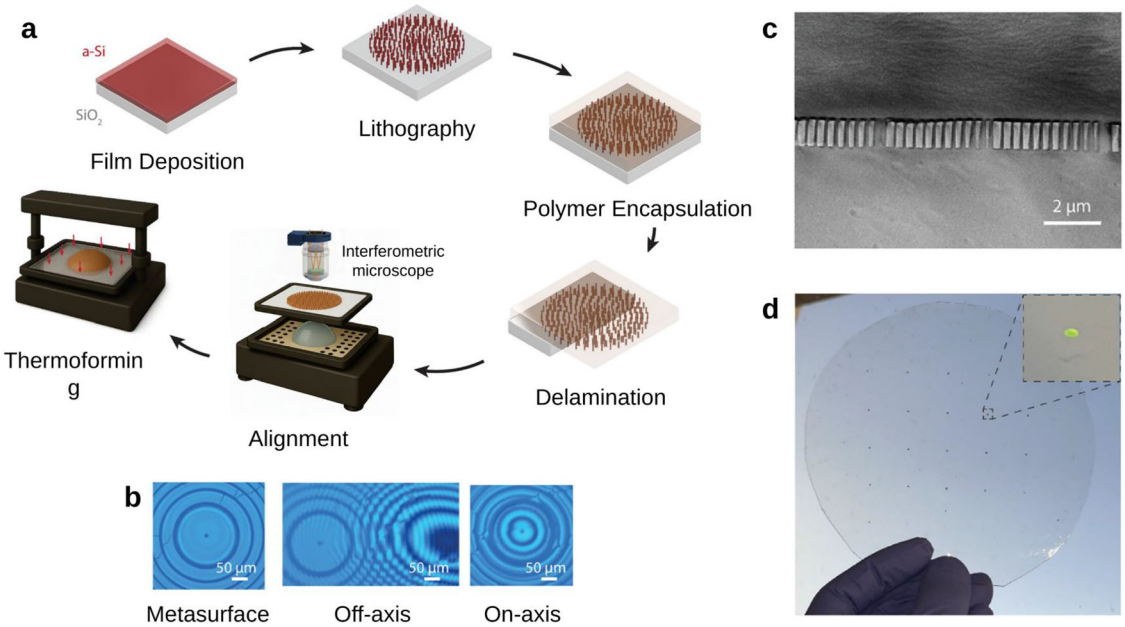


Fig. 1 | Conformal metasurface fabrication and assembly. a Schematic illustration of the fabrication process flow: (1) deposition of metasurface material (here a-Si) onto a handler substrate; (2) patterning of the metasurface using electron beam lithography and plasma etching; (3) encapsulation of the metasurface via spin-coating of a dissolved polymer, followed by thermal bonding to a thicker polymer support sheet of the same material; (4) release of the encapsulated structure by lateral wet etching; (5) alignment of the planar polymer-embedded metasurface over a curved mold using interferometric microscopy; and (6) thermoforming of the metasurface to conform to the mold surface. During alignment, a 480 nm monochromatic light source is used to generate Newton's rings, which serve as fiducial markers. The center of the metasurface phase profile, delineated by visible Fresnel zones, is aligned with the interference fringes to ensure concentric registration. **b** Interferometric microscope images showing (left) the metasurface suspended above the mold with no contact, (middle) misaligned contact between the metasurface and mold, and (right) optimal alignment indicated by concentric interference fringes overlapping with the Fresnel zones. **c** Cross-sectional SEM image of a curved metasurface after thermoforming, confirming structural integrity after the process. **d** Photograph of a 6-inch substrate with an embedded metasurface array fabricated using the proposed process, demonstrating large-area scalability of the process. Inset shows an individual curved metasurface.

substrate containing a 5×5 array of thermoformed metasurfaces, highlighting the scalability of the process. Although electron beam lithography was employed in this proof-of-concept demonstration, the results clearly establish the compatibility of our thermoforming approach with wafer-scale metasurface fabrication workflows, underscoring its potential for large-area production of curved and conformal optical elements.

During the thermoforming process, the metasurface-embedded thermoplastic substrate undergoes substantial viscoelastic deformation. This deformation influences the optical performance of the resulting metasurfaces through two primary mechanisms: changes in the local substrate thickness and variation in the spacing between individual meta-atoms. Quantitative understanding and control of these effects are essential for achieving high-fidelity, optically functional curved and conformal metasurfaces. To this end, we developed a predictive thermorheological model that accurately captures the material response during thermoforming, enabling compensation for deformation-induced optical deviations.

We begin by modeling the thermoforming-induced deformation of a plain thermoplastic sheet—without embedded metastructures—using the Finite Element Method (FEM). The simulation incorporates experimentally measured, temperature-dependent rheological properties of the thermoplastic material, including its shear and loss moduli, as input parameters (Supplementary Note 5). Further simulation details are provided in the "Methods" section and Supplementary Note 6. Figure 2a plots the predicted strain distribution along the radial direction at the top surface of a 200 μm-thick plastic sheet thermoformed over a rotationally symmetric mold with a radius of curvature R = 3.2 mm at 100 °C. To validate the model, we experimentally measured local deformation by tracking the displacement of a sparse rectangular array of silicon islands embedded in the polymer film. The measured strain closely matches the FEM predictions, confirming the accuracy of our modeling framework. Furthermore, strain profiles measured along three orthogonal radial directions (Fig. 2b) reveal excellent symmetry, indicating that the thermoforming process induces uniform, isotropic deformation. This observation validates the model's assumption of axisymmetry and supports the absence of process-induced anisotropy in the resulting structures. Based on first principles estimations, we also proceed to neglect the influence of surface tension in our analysis (Supplementary Note 7).

We further extend our model by incorporating embedded a-Si meta-atoms (assumed to be mechanically rigid) into the thermoplastic substrate to comprehensively characterize thermoforming-induced deformation. To investigate their influence on local strain behavior, we vary the diameters and spacings of the meta-atoms. Figure 2c and 2d show simulated strain profiles for a representative metasurface segment corresponding to a single Fresnel zone at different thermoforming temperatures for optimal design parameters (see Supplementary Note 8 for sub-optimal design). The embedded a-Si meta-atoms, being mechanically rigid relative to the polymer, experience negligible strain, whereas the apparent "sinking" behavior of the thermoplastic between meta-atoms at elevated temperature arises from the viscoelastic flow and sagging of the softened matrix as the composite structure undergoes radial stretching. The results indicate that spatial variations in the volume fill factor of meta-atoms give rise to non-uniform strain distributions, which in turn lead to disproportionate changes in inter-atom spacing across the metasurface. Such strain non-uniformity becomes more pronounced at elevated temperatures, consistent with the decrease in polymer viscosity and the associated increase in local stress redistribution.

We next present our design strategy, which leverages model-predicted strain distributions to adapt the metasurface layout for

https://doi.org/10.1038/s41467-026-77862-w

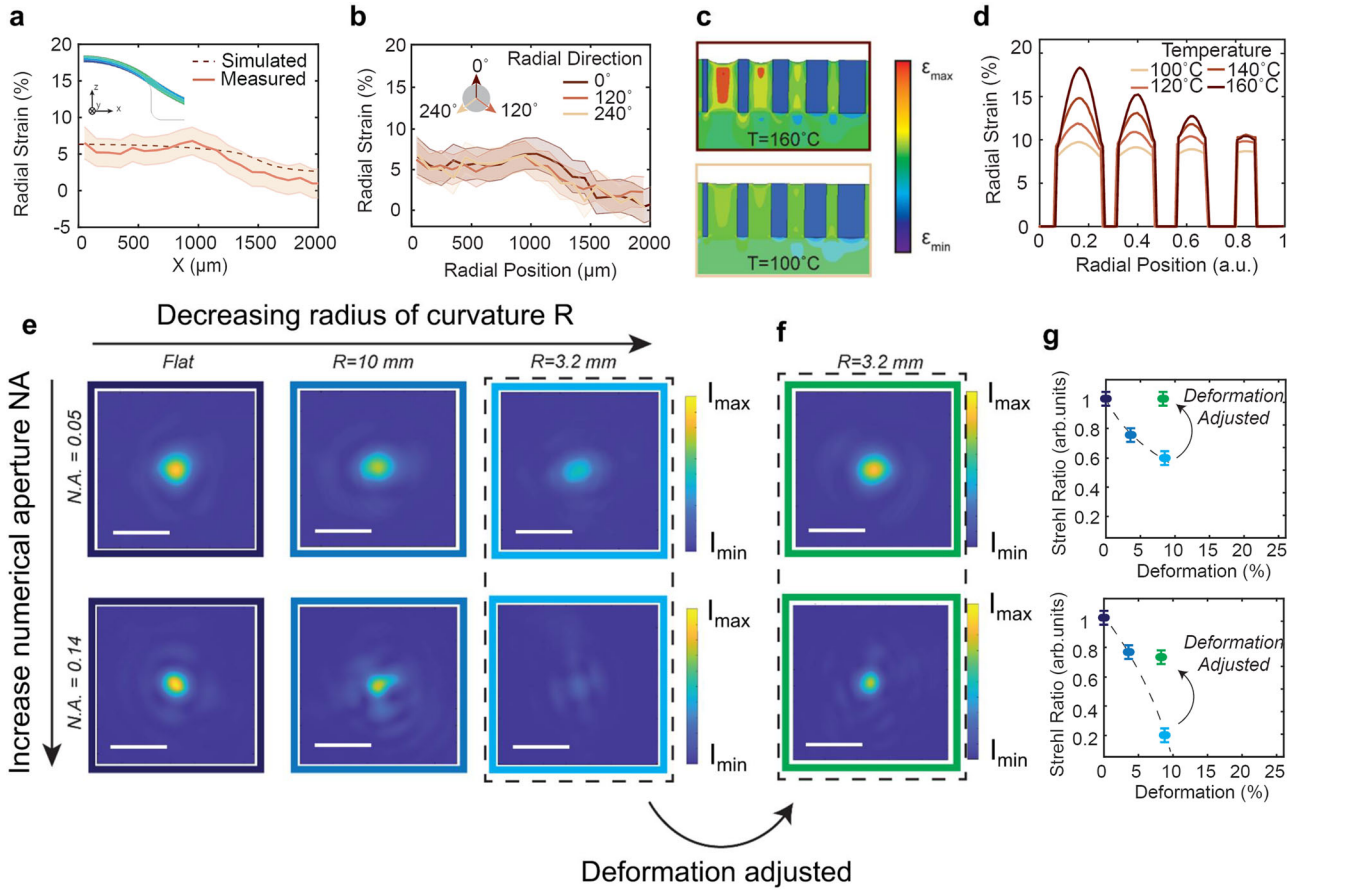


Fig. 2 | Optomechanical behavior of thermoformed curved metasurfaces. a Simulated (dashed line) and measured (solid line) radial strain on the surface of a 200 μm thick polymer sheet thermoformed over a spherical cap with a radius of curvature 3.2 mm at 100 °C, using experimentally extracted rheological parameters. Inset: cross-section of the deformed film profile. **b** Strain profiles measured along three radial directions on the surface, confirming the axisymmetric nature of the deformation process. Shaded regions represent the standard error of the mean. **c** Finite element simulation of radial strain distribution across a single Fresnel zone composed of five meta-atom pillars, at two forming temperatures. At 100 °C (bottom), strain remains symmetric around each meta-atom; at 160 °C (top), strain asymmetry emerges due to enhanced flow and redistribution. The blue (indicating negligible strain) rectangular regions correspond to the a-Si meta-atoms embedded in the PVC matrix. **d** Simulated radial strain profiles at various temperatures, showing that lower thermoforming temperatures result in more uniform strain distributions. **e** Measured PSFs for metalenses of increasing numerical aperture and decreasing radius of curvature without deformation compensation. **f** Measured PSFs of curved metalenses incorporating deformation-compensated design. **g** Simulated (dotted lines) and measured (symbols) Strehl ratios, plotted as a function of strain. Our design, which accounts for the deformation effect, recovers near-diffraction-limited performance.

optimal optical performance under thermoforming-induced deformation. Thermoforming affects metasurface behavior through four principal mechanisms: (1) lateral displacement of meta-atoms, which perturbs the intended optical phase profile; (2) variation in substrate thickness, which modifies local optical path lengths; (3) changes in inter-atom spacing, which influence near-field coupling and alter the optical response of individual meta-atoms; and (4) modification of the local angle of incidence due to surface curvature. To illustrate the impact of uncorrected deformation, we modeled two metalenses—each embedded in a PVC substrate and initially designed for a flat geometry—operating at a wavelength of 940 nm with numerical apertures (NAs) of 0.05 and 0.14, respectively. The design parameters of the meta-atoms and their responses to both in-plane strain and bending-induced deformation are detailed in Supplementary Note 8. Figure 2g shows that the simulated Strehl ratio of the uncorrected metalens decreases monotonically with increasing deformation (dotted line), consistent with experimental measurements (symbols). As expected, metalenses with higher NA exhibit greater susceptibility to performance degradation due to their higher phase gradients, which amplify the effects of deformation-induced phase errors. This degradation is further visualized in Fig. 2e, which shows the measured point spread functions (PSFs) for the two NA designs across increasing curvature conditions. The results highlight the substantial loss of focusing quality at small radii of curvature, particularly for the higher NA design. These findings underscore the importance of incorporating deformation-aware corrections into the metasurface design to preserve optical performance under curved configurations.

To mitigate the performance degradation induced by thermoforming, we implemented a multi-faceted compensation strategy informed by FEM model predictions. Specifically, we adjusted the initial positions of the meta-atoms to offset their displacement during forming and modified the optical phase profile to account for changes in substrate thickness. In parallel, we developed meta-atom designs that are robust to variations in both incident angle and inter-atom spacing, thereby minimizing sensitivity to deformation-induced perturbations (Supplementary Note 8). Figure 2f presents the PSFs of two metalenses incorporating this corrected design. The restored near-diffraction-limited Strehl ratios confirm the effectiveness of our compensation strategy in preserving optical performance despite the large mechanical deformations introduced during thermoforming.

We evaluated the optical performance of a freestanding curved metalens with a numerical aperture (NA) of 0.14 and a radius of curvature $R = 3.2$ mm, designed to operate at a wavelength of 940 nm and fabricated using the thermoforming method. The deformation

compensation strategy described in the previous section was applied during the design process. Figure 3a shows a schematic of the device under collimated illumination. To assess focusing performance, we experimentally characterized the 3D PSF of the metalens. Figure 3b and 3c present the measured intensity distributions in the *x*-*z* and *x*-*y* planes, respectively, alongside simulation of an ideal curved lens without fabrication imperfections (Fig. 3d). The metalens demonstrates diffraction-limited performance, with a Strehl ratio of 0.89 (Fig. 3e) and an MTF closely matching that of the ideal aberration-free design (Fig. 3f). Additional analysis of the aberration contributions based on Zernike decomposition of the reconstructed wavefront is provided in Supplementary Note 9.

As a next demonstration, we evaluated a conformal refractive-metasurface hybrid lens, fabricated using an off-the-shelf plano-convex lens as the mold. Through thermoforming, the metasurface layer was conformally bonded onto the curved surface of the refractive lens, forming an integrated hybrid optical system. Such hybrid optics offer unique performance advantages by combining the precise monochromatic aberration correction enabled by metasurfaces with the large group delay inherent to refractive lenses—critical for broadband achromatic operation.

As a proof-of-concept, we fabricated a hybrid lens shown in Fig. 4g, in which the metasurface is designed to enhance the refractive power of the underlying lens. The bare refractive lens depicted in Fig. 4a has a focal length of $f_1 = 3.4$ mm, which is reduced to $f_2 = 1.8$ mm after metasurface integration. Experimentally measured intensity distributions around both focal planes are presented in the lower panels of Fig. 4a and 4b. The hybrid lens exhibits a peak intensity ratio of $I_1 / I_2 = 80$ at the two focal planes f_1 and f_2, demonstrating exceptionally high contrast between the desired (first-order) and residual (zeroth-order) diffraction of the conformal metasurface. This result underscores the effectiveness of our fabrication and deformation-compensation strategies. We further characterized the hybrid lens's focusing performance at the f_2 focal plane. The measured PSF (Fig. 4c) shows good agreement with simulations (Fig. 4d), yielding a Strehl ratio of 0.72 according to Fig. 4e. The results indicate that the conformal hybrid lens operates near the diffraction limit.

Insect compound eyes consist of thousands of microlenses, each typically tens to hundreds of micrometers in diameter, arranged in a hemispherical array configuration. This unique architecture enables a wide field of view by distributing independent optical apertures across a curved surface, while the small size of each individual aperture

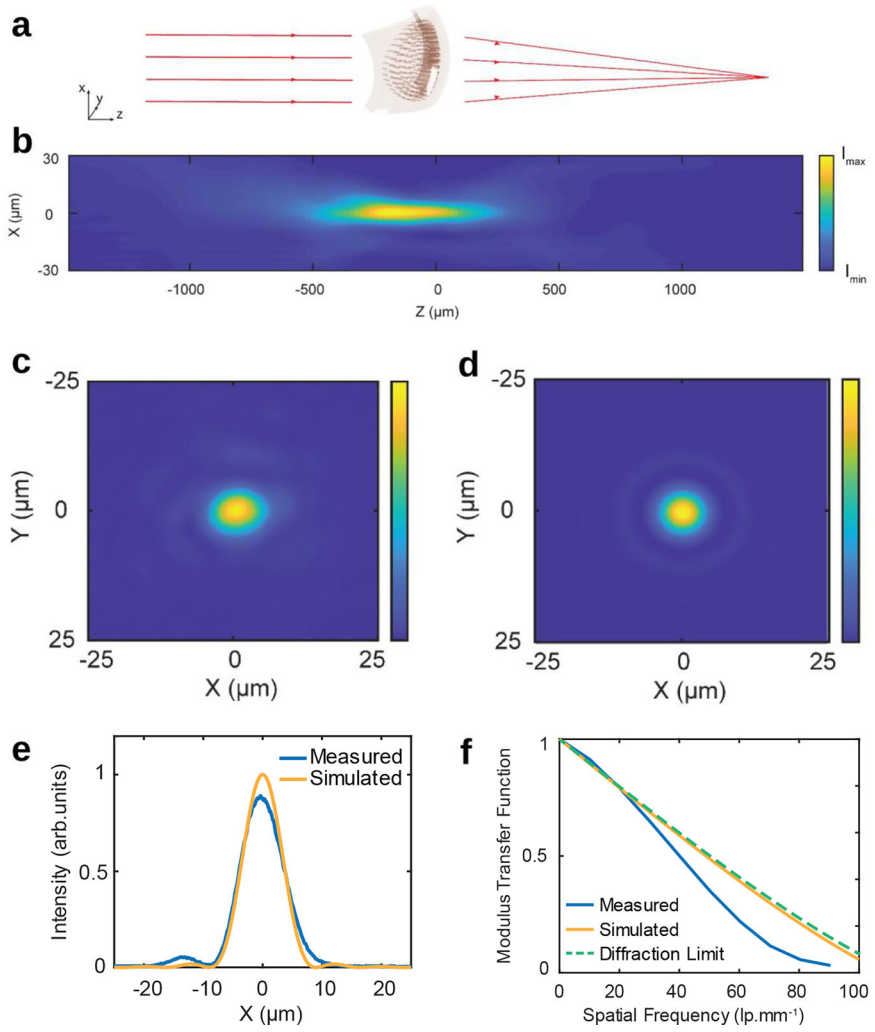


Fig. 3 | Experimental characterization of a freestanding curved metalens. **a** Schematic illustrating the operation of the curved metalens under collimated monochromatic illumination. **b** Measured optical intensity distribution along the optical (*z*) axis, captured in the *x*-*z* plane. (**c**-**d**) PSF intensity maps at the focal plane (f = 7 mm): **c** experimental measurement and (**d**) simulated reference, showing close agreement. **e** PSF line profile along the *x*-direction at the focal plane, comparing experimental data (blue) and simulation (orange). **f** MTF as a function of spatial frequency: (green dashed line) theoretical diffraction limit; (orange line) simulated MTF for the lens; (blue line) experimentally retrieved MTF obtained via inverse Fourier transform of the measured PSF. The results confirm near-diffraction-limited performance of the curved metalens.

https://doi.org/10.1038/s41467-026-77862-w

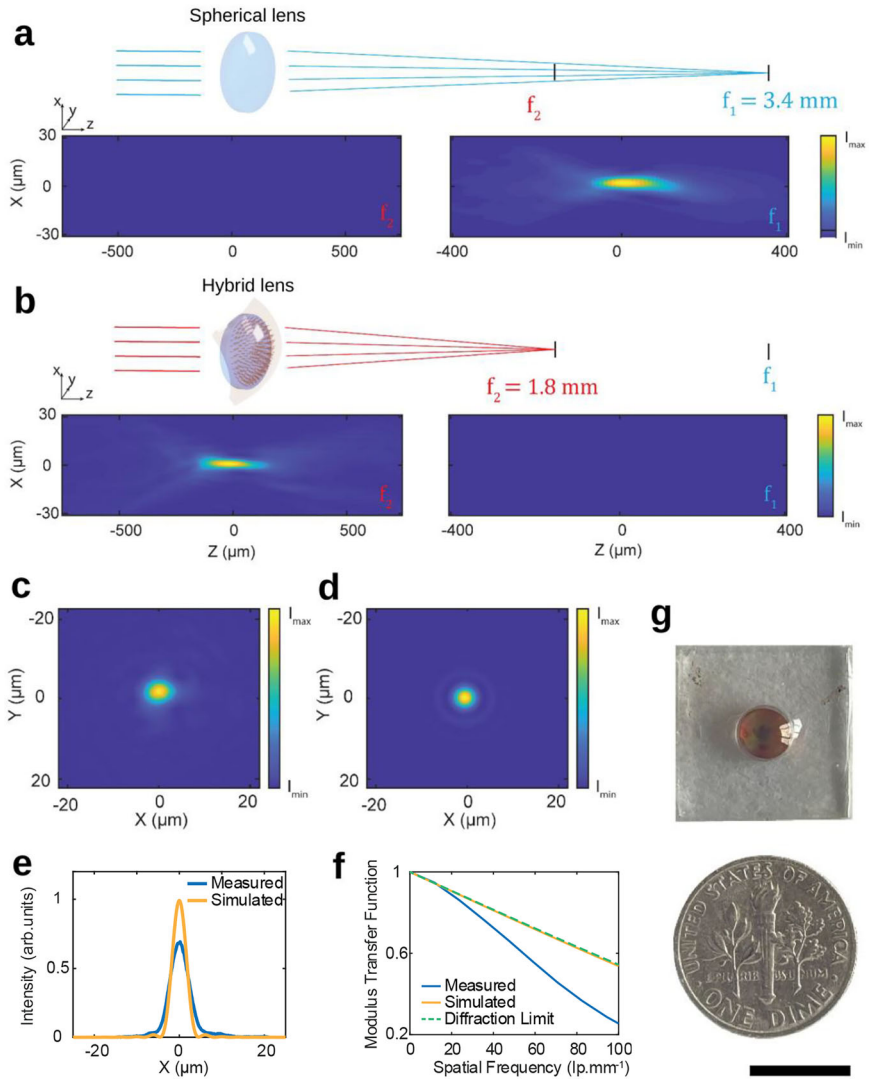


Fig. 4 | Experimental demonstration of a hybrid refractive-metasurface optic. Schematics and measured intensity distributions along the optical axis under collimated monochromatic illumination for (**a**) a plano-convex spherical lens (focal length $f_1 = 3.4$ mm, NA = 0.10) and (**b**) a hybrid optic consisting of the same spherical lens conformally integrated with a thermoformed metalens, reducing the effective focal length to $f_2 = 1.8$ mm (NA = 0.18). Cross-sectional intensity distributions of the PSF at the focal plane of the hybrid optic: (**c**) experimental measurement and (**d**) simulation, showing close agreement. **e** PSF line scan across the focal spot, comparing experiment (blue) and simulation (orange). **f** MTF of the hybrid optic: (green dashed line) diffraction limit; (orange line) simulated performance; (blue line) experimental MTF obtained via Fourier transform of the measured PSF. **g** Photograph of the hybrid optic shown next to a U.S. dime for scale.

inherently yields low aberrations and a large depth of field. The wide field of view and large depth of field collectively contribute to high motion sensitivity, allowing insects to detect fast-moving objects across a broad visual field within a remarkably compact form factor (Fig. 5a). These characteristics have long made insect compound eyes a compelling biological model for artificial vision systems[24,25]. However, traditional microlens-based artificial compound eyes fabricated via direct laser lithography[26], thermal transforming[27], and pneumatic deformation[28] often suffer from non-uniform lens deformation and limited scalability when transformed into curved geometries, which in turn degrade overall imaging performance. To address these challenges, we fabricated a curved metalens compound eye by transforming a flat metalens array (Fig. 5b-c). Our design strategy provides precise control of the lens curvature across the entire array, enabling stable and uniform image quality from the central to peripheral regions (further details are provided in Supplementary Notes 10 and 11).

We conducted image demonstrations with the curved metalens compound eye to verify its ability to produce high-quality compound eye images across the entire metalens array. The system generated well-focused images of a checkerboard pattern at working distances ranging from 2 cm to 10 cm, demonstrating a large depth of field (Fig. 5d). We next established an optical setup for object imaging under angular variation to quantify the compound eye's full field of view, as described in detail in the Methods section (see Supplementary Note 12). The curved metalens compound eye produced uniform sub-aperture images of the letter 'E' object at incident angles of 0°, 15°, and 30° (Fig. 5e-g), with clearly distinguishable edges and line features reproduced across all viewing angles. In particular, the contrast profiles in Fig. 5h remained stable across all angles, confirming conformal fabrication of the metalenses in both central and peripheral regions.

Discussion

We have developed and experimentally validated a thermoforming-based strategy for the fabrication of curved and conformal metasurfaces. Leveraging an industry-standard process, our approach achieves wafer-scale scalability while maintaining micron-level alignment accuracy and millimeter-scale radii of curvature. Through

https://doi.org/10.1038/s41467-026-77862-w

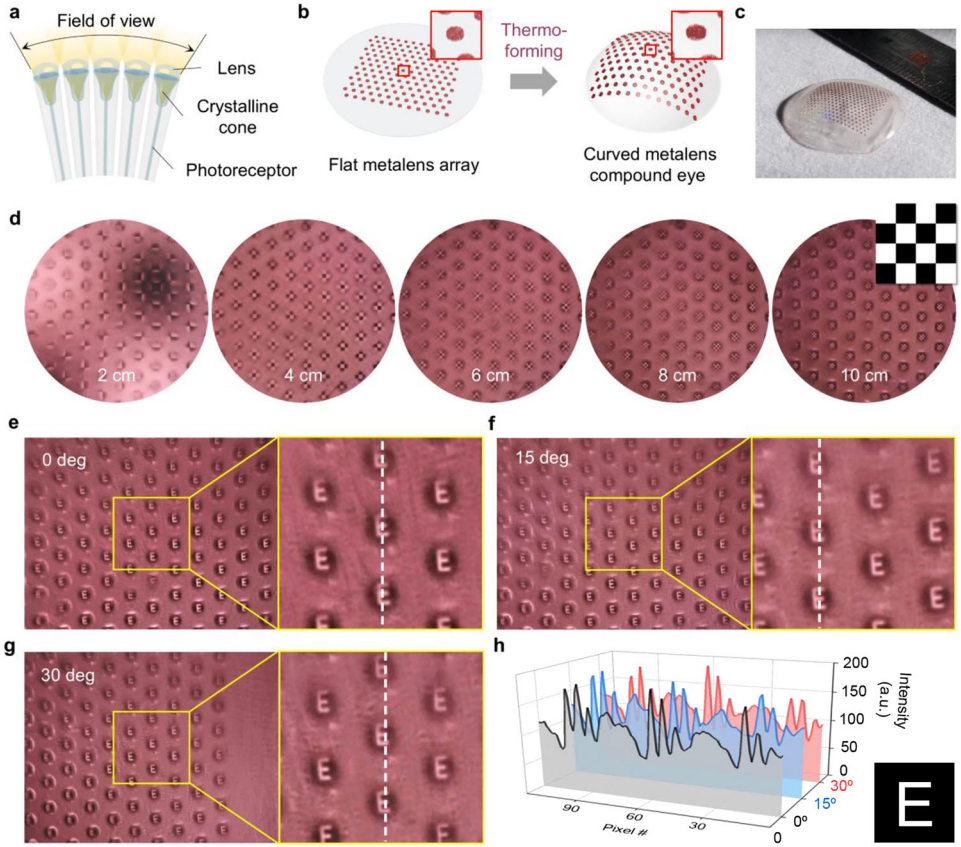


Fig. 5 | Imaging demonstration of a conformal metalens compound eye. **a** Schematic of an insect compound eye, consisting of multiple microlenses coupled to crystalline cones and photoreceptors, enabling a wide field-of-view. **b** Schematic of the thermoforming process, transforming a flat metalens array into a curved metalens compound eye. **c** Photograph of the fabricated curved metalens compound eye, shown next to a ruler for scale. **d** Imaging results of the curved metalens compound eye for a checkerboard target at varying working distances. The checkerboard target size is 2 cm by 2 cm. Imaging results of the letter "E" under different incident angles: **e** 0°, **f** 15°, and **g** 30°. Insets show magnified views of the captured images, with dotted lines marking the locations used for intensity profiling. The linewidth of the letter "E" is 2.5 mm. The scale bars are 500 μm. **h** Line intensity profiles extracted along the dotted lines in (**e**–**g**), demonstrating consistent image contrast across both central and peripheral regions of the array, confirming uniform optical performance of the compound eye.

systematic thermorheological modeling, we established a predictive framework to compensate for deformation-induced optical errors, enabling devices with diffraction-limited performance.

We demonstrated the versatility of this platform by realizing freestanding curved metalenses, conformal refractive-metasurface hybrid optics, and a bioinspired compound eye. In each case, our results highlight the ability to preserve structural integrity, achieve high focusing fidelity, and deliver uniform imaging performance across the entire aperture. Importantly, the use of rigid thermoplastic sheets ensures compatibility with standard wafer-level lithography, including DUV and nanoimprint techniques, thus providing a direct pathway toward large-area, high-throughput manufacturing.

Beyond device-level demonstrations, the predictive thermorheological modeling framework established in this work provides the basis for a digital twin approach to conformal meta-optics. By integrating mechanical deformation modeling, electromagnetic simulation, and fabrication parameter control within a unified virtual environment, high-fidelity digital replicas of thermoformed metasurfaces can be constructed. Such digital twins enable pre-fabrication optimization, tolerance analysis, yield prediction, and closed-loop process refinement. In an industrial setting, this capability can significantly reduce development cycles, improve reproducibility, and facilitate scalable deployment of conformal photonic systems.

Compared to existing approaches based on direct writing, soft stamping, or elastomer transfer, thermoforming uniquely combines precision, robustness, and scalability. By decoupling optical design from geometric constraints, our method opens opportunities for integrating conformal metasurfaces into compact, wide-angle, and multifunctional optical systems. The demonstrated wafer-scale compatibility establishes thermoforming as a practical and industrially viable solution for next-generation conformal photonics, with applications ranging from wearable optics, including augmented reality glasses and flexible displays, to bioinspired vision systems for robotics and beyond.

Methods

Metasurface fabrication

The fabrication process begins with a (100)-oriented silicon wafer (University Wafers, Inc.) as the substrate. A 180 nm-thick phosphate glass layer (Spin-on-Glass P-280HP, Desert Silicon) is spin-coated onto the wafer and annealed at 220 °C for 10 min. Subsequently, 100 nm of SiO_2 and 975 nm of a-Si are deposited via plasma-enhanced chemical vapor deposition (SAMCO, Inc.) at 350 °C and 270 °C, respectively. The metasurface pattern is defined using electron beam lithography (HS-50, STS-Elionix) operated at 50 kV beam voltage and 10 nA current. The pattern is written onto a 320 nm-thick ma-N 2403 negative-tone electron beam resist (Microresist Technology), spin-coated at 3000 rpm for 1 minute and soft-baked at 90 °C for 2 minutes. Prior to resist application, the substrate is treated with hexamethyldisilazane (HMDS) vapor to enhance adhesion. To suppress charging effects during exposure, a layer of water-soluble conductive polymer (ESpacer 300Z, Showa Denko America, Inc.) is applied over the resist. Post-

exposure, the resist is developed in a tetramethylammonium hydroxide (TMAH)-based developer (AZ 726 MIF, Microchemicals). Pattern transfer into the a-Si layer is achieved via reactive ion etching (RIE; Pegasus, SPTS Technologies) using alternating cycles of SF_6 and C_4F_8. After etching, the remaining resist is removed by oxygen plasma ashing. For encapsulation, a PVC solution is prepared by dissolving 10 g of polyvinylchloride (PVC) in 100 mL of cyclohexanone. This solution is spin-coated onto the metasurface at 1500 rpm for 40 s with a ramp rate of 100 rpm/s, followed by annealing at 130 °C for 5 min. The encapsulation is repeated using a higher concentration solution (20 g PVC in 100 mL cyclohexanone), resulting in a total encapsulation layer thickness of ~10 μm. A PVC sheet (Sigma-Aldrich, Inc.) is then thermally bonded onto the encapsulated surface by annealing at 150 °C. To release the structure, the sample is immersed in a 1:1 mixture of 25% hydrofluoric acid (HF) and isopropyl alcohol (IPA), which selectively dissolves the underlying phosphate glass and SiO_2 layers. Once delaminated, the freestanding metasurface-embedded PVC sheet is rinsed with deionized water, blow-dried, and allowed to dry completely under ambient conditions.

Cross-sectional scanning electron microscopy sample preparation

Samples were prepared for cross-sectional imaging (Fig. 1c) by embedding the polymer sheet in a low-viscosity epoxy resin (Epofix, Struers). The sheet was positioned vertically in a mounting mold such that the thickness direction was exposed. Liquid epoxy was then poured, and the assembly was placed under vacuum to facilitate resin infiltration and remove trapped air. After curing at room temperature, the mounted sample was mechanically pre-polished to obtain a flat cross section through the center of the metasurface region. Final surface preparation was carried out using low-energy argon ion polishing with a Gatan Model 691 Precision Ion Polishing System (Gatan, Inc.). Polishing was performed at shallow incidence angles (< 10°) and low ion energies (< 1 keV), with intermittent milling steps to minimize local heating and reduce deformation of the polymer matrix.

Due to the curved geometry of the PVC substrate, it is difficult to ensure that the sectioning plane is perfectly perpendicular to the local surface. As a result, the apparent variation in meta-atom width observed in Fig. 1c arises from oblique sectioning of the cylindrical structures rather than from any deformation or degradation of the meta-atoms during the thermoforming process.

Thermoforming

Prior to thermoforming, the thermoplastic substrate is mounted onto a concentric metal support ring (Xometry Inc.) to ensure mechanical stability and handling ease. This clamped assembly forms a circular sheet that is fixed at the boundary and free elsewhere. The assembly is positioned above a rigid curved mold bonded using UV-curable adhesive (OrmoComp, MicroResist GmbH) to a perforated metal base that enables vacuum suction during forming. The thermoplastic sheet and mold are initially brought into near contact without applying pressure.

The entire setup is placed under an interferometric microscope equipped with a monochromatic blue light source ($\lambda = 480$ nm), a 50× interferometric objective, and a bandpass filter (center wavelength 488 nm, full-width at half-maximum 10 nm; Thorlabs Inc.). The position of the mold base is finely adjusted relative to the support ring until concentric Newton's rings are centered over the metasurface region, indicating precise lateral alignment. Once alignment is achieved, the relative positions of the base and support ring are fixed using either mechanical clamps or UV-curable adhesive.

The aligned assembly is then transferred to a commercial benchtop thermoforming system (FormBox, Mayku Inc.), which provides primarily top-side radiative heating. To suppress convective heat loss and improve thermal uniformity, the sample, clamping rings, mold, and support plate are enclosed during heating. Specifically, the polymer sheet and clamp assembly are covered by an aluminum-foil-lined enclosure, while the interior walls of the FormBox are shielded and the perforated base is sealed from below to prevent airflow through the vacuum holes. This configuration minimizes convective currents and promotes heat transfer dominated by radiation from above and lateral conduction through the metallic components, resulting in a gradual and spatially uniform temperature increase.

The temperature of the assembly is monitored using two thermocouples attached to the metallic clamping ring. Due to the large thermal mass of the metal components and enclosure, the thermal response is slow and smooth, and the measured temperature provides a reliable proxy for the polymer temperature. Heating is typically performed at a rate of approximately 3 °C/min. After reaching approximately 100 °C, the system is held isothermally for 5 minutes to ensure thermal equilibration of the entire metal-polymer assembly.

Forming is initiated by applying vacuum from below, with an estimated pressure differential of 5–10 kPa based on the nominal performance of the FormBox system. Initial contact and deformation occur rapidly (~ 1 s), followed by full conformity to the mold over several seconds. After forming, the assembly is allowed to cool in air. Upon removal of the thermal enclosure, the temperature decreases from ~100 °C to ~60 °C within ~10 s, and then to ~40 °C over an additional minute, resulting in an accelerated cooling rate once the sample is exposed to ambient conditions.

Thermorheological characterization and modeling

To simulate microstructural deformation during thermoforming, we first experimentally measured the rheological properties of the PVC substrate. Dynamic mechanical analysis (ARES-G2, TA Instruments) was performed using a 2° cone-plate geometry to obtain the storage and loss moduli of the PVC sheet. Angular frequency sweeps were conducted over the range of 0.3–100 rad/s following a 5-minute thermal stabilization period. The resulting viscoelastic parameters were fitted using the MCalibration software (PolymerFEM, Ansys Inc.) based on a linear elastic model with a fifth-order Prony series representation.

The deformation behavior was simulated using a dynamic implicit solver implemented in the Abaqus finite element modeling package (Simulia, Dassault Systèmes). Exploiting the axial symmetry of the system, a 2-D cross-sectional model of the thermoforming setup—including the PVC substrate, mold, support ring, and metal base—was constructed. The mold and metal base were modeled as rigid wire bodies fixed at reference points, while the PVC sheet was represented as a shell element, constrained at its contact point with the mold apex (initial alignment point) and at the inner edge of the concentric support ring. A vacuum load of 8 kPa was applied over a 5-second ramp, unless otherwise specified. Tangential contact interactions were defined with a standard friction coefficient of 0.3, while normal contact behavior was modeled as hard contact. A surface-to-surface discretization scheme was employed using a finite-sliding formulation, with contact stabilization enabled and a relative penetration tolerance set to 0.001. Deformation profiles were extracted along the radial direction and mapped against corresponding radial coordinates. For spatial resolution, a mesh size of 10 μm was used for the bulk substrate, while a refined mesh of 10 nm was applied in regions capturing microstructural deformation near the metasurface.

Optical measurement

Optical measurements were conducted using a 940 nm continuous-wave laser diode module (LQC940-90E, Newport Inc.) as the light source. The laser beam was first expanded using a beam expander (ZBE22, Thorlabs Inc.), then directed onto the conformal optics sample, which was mounted on a three-axis translational stage equipped with a two-angle tilt mount for precise orientation adjustment. The focused light from the sample was collected using a standard 50×

microscope objective and projected onto a high-resolution near-infrared camera (Alvium 1800 U-501m NIR, Allied Vision Inc., 2592 × 1944 pixels). The camera and objective assembly were mounted on a separate three-axis translational stage. To obtain the three-dimensional optical intensity distribution, the z-position of the detection assembly was incrementally swept, capturing a sequence of x-y sections at different depths to reconstruct the 3-D PSF.

The compound eye imaging experiments were conducted using a 780 nm collimated laser diode module (CPS780S, Thorlabs Inc.) with a plano-concave lens with a focal length of 150 mm (KPC031, Newport Corporation) to expand the light beam and fully illuminate the object mask. For the angular imaging experiments, a letter "E" mask with a linewidth of 2.5 mm was used as the imaging target. A ground-glass diffuser (#47-953, Edmund Optics Inc.) was inserted between the lens and the object mask to ensure uniform illumination. The focused metalens images from the curved metalens compound eye were relayed via a 1:1 relay lens (MAP107575-A, Thorlabs Inc.) onto a CMOS image sensor (Sony IMX477R, 12.3MP, Sony Semiconductor Solutions Corporation). Imaging at different incident angles was carried out by rotating the object relative to the central curvature point of the curved metalens compound eye, ensuring that the rotation axis coincided with the array's geometric center.

Data availability

All data supporting the findings of this study are available within the paper and its Supplementary Information.

References

1. Zhou, Y. et al. Flexible Metasurfaces for Multifunctional Interfaces. *ACS Nano* **18**, 2685–2707 (2024).
2. Walia, S. et al. Flexible metasurfaces and metamaterials: a review of materials and fabrication processes at micro- and nano-scales. *Appl. Phys. Rev.* **2**, 011303 (2015).
3. Geiger, S. et al. Flexible and stretchable photonics: the next stretch of opportunities. *ACS Photonics* **7**, 2618–2635 (2020).
4. Burckel, D. B., Sweatt, W. C. & Reinke, C. M. Exploring curved metasurface optics. in *2024 IEEE Research and Applications of Photonics in Defense Conference, RAPID 2024 - Proceedings* (Institute of Electrical and Electronics Engineers Inc. https://doi.org/10.1109/RAPID60772.2024.10646914 2024).
5. Aieta, F., Genevet, P., Kats, M. & Capasso, F. Aberrations of flat lenses and aplanatic metasurfaces. *Opt. Express* **21**, 31530–31539 (2013).
6. Han, N., Huang, L. & Wang, Y. Illusion and cloaking using dielectric conformal metasurfaces. *Opt. Express* **26**, 31625–31635 (2018).
7. Wu, K., Coquet, P., Wang, Q. J. & Genevet, P. Modelling of free-form conformal metasurfaces. *Nat. Commun.* **9**, 3494 (2018).
8. Nikolov, D. K. et al. Metaform optics: bridging nanophotonics and freeform optics. *Sci. Adv.* **7**, eabe5112 (2021).
9. Yang, F. et al. Wide field-of-view metalens: a tutorial. *Adv. Photonics* **5**, 033001 (2023).
10. Cheng, J., Jafar-Zanjani, S. & Mosallaei, H. All-dielectric ultrathin conformal metasurfaces: lensing and cloaking applications at 532 nm wavelength. *Sci. Rep.* **6**, 38440 (2016).
11. Zhang, W., Zuo, B., Chen, S., Xiao, H. & Fan, Z. Design of fixed correctors used in conformal optical system based on diffractive optical elements. *Appl. Opt.* **52**, 461–466 (2013).
12. Wang, Y. et al. Wearable plasmonic-metasurface sensor for non-invasive and universal molecular fingerprint detection on biointerfaces. *Sci. Adv.* **7**, eabe4553 (2021).
13. Gan, Y. et al. See-Through Conformable Holographic Metasurface Patches for Augmented Reality. *Laser Photon. Rev.* **19**, 2401240 (2024).
14. Kang, M. et al. Photochemically engineered large-area arsenic sulfide micro-gratings for hybrid diffractive–refractive infrared platforms. *Adv. Photonics Res.* **5**, 2300241 (2024).
15. Bhingardive, V., Menahem, L. & Schvartzman, M. Soft thermal nanoimprint lithography using a nanocomposite mold. *Nano Res.* **11**, 2705–2714 (2018).
16. Kim, G. et al. Metasurface-driven full-space structured light for three-dimensional imaging. *Nat. Commun.* **13**, 5920 (2022).
17. Choi, H. et al. Realization of high aspect ratio metalenses by facile nanoimprint lithography using water-soluble stamps. *PhotoniX* **4**, 18 (2023).
18. Kamali, S. M., Arbabi, A., Arbabi, E., Horie, Y. & Faraon, A. Decoupling optical function and geometrical form using conformal flexible dielectric metasurfaces. *Nat. Commun.* **7**, 11618 (2016).
19. Shi, Y. et al. Flexible multilayer metasurfaces: design and applications on foldable and conformable substrates. *Adv. Mater. Technol.* **10**, 2402130 (2025).
20. Kamali, S. M., Arbabi, E., Arbabi, A., Horie, Y. & Faraon, A. Highly tunable elastic dielectric metasurface lenses. *Laser Photon. Rev.* **10**, 1002–1008 (2016).
21. Ee, H.-S. & Agarwal, R. Tunable metasurface and flat optical zoom lens on a stretchable substrate. *Nano Lett.* **16**, 2818–2823 (2016).
22. Burch, J. & Di Falco, A. Holography using curved metasurfaces. *Photonics* **6**, 8 (2019).
23. Zhang, X., Cai, H., Daqiqeh Rezaei, S., Rosenmann, D. & Lopez, D. A universal metasurface transfer technique for heterogeneous integration. *Nanophotonics* **12**, 1633–1642 (2023).
24. Land, M. F. & Nilsson, D.-E. *Animal Eyes*. (Oxford University Press, 2012).
25. Prone, G. et al. Scalable, nanometer-accurate fabrication of all-dielectric metasurfaces with narrow resonances tunable from near infrared to visible wavelengths. *Adv. Photonics Res.* **3**, 2200014 (2022).
26. Wang, L. et al. Holographic laser fabrication of 3D artificial compound μ-eyes. *Light.: Adv. Manuf.* **4**, 339–347 (2024).
27. Deng, Z. et al. Dragonfly-eye-inspired artificial compound eyes with sophisticated imaging. *Adv. Funct. Mater.* **26**, 1995–2001 (2016).
28. Luo, J., Guo, Y., Wang, X. & Fan, F. Design and fabrication of a multi-focusing artificial compound eyes with negative meniscus substrate. *J. Micromech. Microeng.* **27**, 045011 (2017).
29. Ni, X., Wong, Z. J., Mrejen, M., Wang, Y. & Zhang, X. An ultrathin invisibility skin cloak for visible light. *Science* **349**, 1310–1314 (2015).
30. Kim, K., Yoon, G., Baek, S., Rho, J. & Lee, H. Facile nanocasting of dielectric metasurfaces with sub-100 nm resolution. *ACS Appl. Mater. Interfaces* **11**, 26109–26115 (2019).
31. Kim, J. et al. A water-soluble label for food products prevents packaging waste and counterfeiting. *Nat. Food* **5**, 293–300 (2024).
32. Burch, J. & Di Falco, A. Surface topology specific metasurface holograms. *ACS Photonics* **5**, 1762–1766 (2018).
33. Biabanifard, M., Xiao, J. & Di Falco, A. Thin-film polymeric metasurfaces for visible wavelengths. *Appl. Phys. Lett.* **123**, 231702 (2023).
34. Ko, J. et al. Metasurface-embedded contact lenses for holographic light projection. *Adv. Sci.* **11**, 2407045 (2024).

Acknowledgements

This work was carried out in part through the use of MIT.nano shared experimental facilities.

Author contributions

L.M. performed finite element modelling, developed fabrication protocols, and characterized the metasurface optics. S.C. designed and characterized the compound eye micro-metalens array. J.E.F., L.R., K.P.D., A.U., and J.X.B.S. contributed to device fabrication. Z.L., H.Z., and P.B. assisted with metasurface optics testing. J.H. conceived the study. T.G., Y.M.S., A.M., and J.H. supervised and coordinated the research. J.H., L.M., S.C., and Y.M.S. drafted the manuscript. All authors contributed to technical discussions and writing the paper.

Funding
This work was sponsored by the DARPA ENVision program, the Inno-CORE program of the Ministry of Science and ICT (GIST InnoCORE KH0830) and by the National Research Foundation of Korea (NRF) grant funded by the Korea government (MSIT). The views, opinions and/or findings expressed are those of the authors and should not be interpreted as representing the official views or policies of the Department of Defense or the U.S. Government.

Competing interests
L.M., L.R., T.G., and J.H. are inventors on a pending U.S. patent application (U.S. Patent Application No. 63/387,582) related to the fabrication technology described in this manuscript. The patent application has been licensed to 2Pi Inc. H.Z., P.B., T.G., and J.H. hold equity interests in 2Pi Inc. The remaining authors declare no competing interests.

Additional information
Supplementary information The online version contains supplementary material available at https://doi.org/10.1038/s41467-026-77862-w.

Correspondence and requests for materials should be addressed to Zhaoyi Li, Tian Gu or Young Min Song.

Peer review information *Nature Communications* thanks Hongyoon Kim and the other anonymous reviewers for their contribution to the peer review of this work. A peer review file is available.

Reprints and permissions information is available at http://www.nature.com/reprints

Publisher's note Springer Nature remains neutral with regard to jurisdictional claims in published maps and institutional affiliations.

Open Access This article is licensed under a Creative Commons Attribution-NonCommercial-NoDerivatives 4.0 International License, which permits any non-commercial use, sharing, distribution and reproduction in any medium or format, as long as you give appropriate credit to the original author(s) and the source, provide a link to the Creative Commons licence, and indicate if you modified the licensed material. You do not have permission under this licence to share adapted material derived from this article or parts of it. The images or other third party material in this article are included in the article's Creative Commons licence, unless indicated otherwise in a credit line to the material. If material is not included in the article's Creative Commons licence and your intended use is not permitted by statutory regulation or exceeds the permitted use, you will need to obtain permission directly from the copyright holder. To view a copy of this licence, visit http://creativecommons.org/licenses/by-nc-nd/4.0/.

© The Author(s) 2026